Ablation and spallation of gold films irradiated by ultrashort laser pulses

Brian J. Demaske,[1] Vasily V. Zhakhovsky,[1] Nail A. Inogamov,[2] and Ivan I. Oleynik[1]
[1]*Department of Physics, University of South Florida, Tampa, Florida 33620, USA*
[2]*Landau Institute for Theoretical Physics, RAS, Chernogolovka 142432, Russia*
(Received 5 August 2010; published 25 August 2010)

By extending molecular-dynamics simulation to the experimental micrometer length scale, we observed the complete dynamics of gold films subjected to ultrashort ($\lesssim 1$ ps) laser irradiation, culminating in cavitation then ablation of the melt at the front, and crack nucleation then spallation at the rear side of the sample. For thick films (>0.5 μm) ablation and spallation are spatially separated; whereas for thin films, they merge into a unique damage process, which leads to a dependence of ablation threshold on film thickness. This work provides insights into thermomechanical dynamics of irradiated metal films, including coupling-decoupling of ablation and spallation processes, and opens up a field of direct comparison between experiment and atomistic simulations.

DOI: 10.1103/PhysRevB.82.064113 PACS number(s): 79.20.Eb, 02.70.Ns

I. INTRODUCTION

Ultrashort laser pulse (usLP) interactions with metals have been intensively studied in the last decade due to novel applications such as thin film deposition and surface micromachining, for reviews see Ref. 1. In addition, usLP experiments provide unique opportunities to explore the fundamental mechanisms of materials response to ultrahigh strain rates produced by usLP heating.[2–7] The mechanisms of ablation and spallation caused by nanosecond laser irradiation are now well understood.[8,9] A well-established feature of nanosecond ablation is that it is *an inherently thermal process* associated with high-rate evaporation of the material and plasma formation. However, spallation is not thermal but mechanical in nature, and is caused by the tensile wave reflected off the target's rear surface. The spallation dynamics of targets subjected to comparable strain rates were also studied in flyer-plate experiments.[10,11]

In contrast, the fundamental atomic-scale mechanisms of materials response to usLP are not well understood. Although it is accepted that both ablation and spallation induced by usLP with pulse duration $\lesssim 1$ ps are *mechanical* in nature,[12–20] the possibility of their coupling in thin films was considered neither experimentally nor theoretically. Such a possibility exists because for a thin-enough film the superposition of rarefaction waves reflected from the frontal and rear free surfaces may exceed the tensile strength of the material thereby resulting in fracture damage. By increasing film thickness to values well above the sum of the ablated and spalled layers, the ablation-spallation processes become decoupled. Study of these new phenomena by molecular-dynamics (MD) simulations that allow for direct comparison to experiment is quite challenging due to the requirement of very large samples.

By extending MD simulation to the experimental micrometer length scale, we observed the concerted dynamics of ablation and spallation in a single metal film subjected to usLP irradiation. The increased capabilities of MD allow for an accurate microscopic description of the time-resolved sequence of coupled events within the film, including isochoric pressure buildup in the frontal part, acoustic formation of compression and tensile waves, melting, void nucleation in molten gold, and plastic deformation and fracture damage of crystal culminating in ablation at the front and spallation at the rear of the film. The system under study is gold film irradiated by usLP, for which experimental data (ablated crater depth and absorbed fluence threshold) are available.[7] By comparing the simulated ablation fluence threshold with one obtained from experiment this work provides a reliable validation of the microscopic picture of materials response to usLP irradiation that is not currently available from experiment.

II. COMPUTATIONAL MODEL

The interaction of usLP with metal can be divided into two consecutive stages. The initial short-duration stage includes the formation of a heated and highly pressurized frontal layer upon the absorption of laser energy, and its distribution through the target. The subsequent long-duration stage involves a complex material transformation that is due to decomposition of the initial pressurized state. At the onset of the short-duration stage, the energy from the usLP is absorbed by the conduction electrons within a skin layer of 10 nm.[8] The thermal energy from these electrons then propagates into the target thereby heating the ions. The electron-ion thermalization process in gold has a characteristic time $\tau_{ie} \sim 5$ ps, and electrons reach thermal equilibrium with the ions during $\tau \sim 4\tau_{ie} \sim 20$ ps, which is roughly one-third the acoustic time $\tau_s = d_T / c_s$, where d_T is the heating depth and c_s is the sound speed of the material. Because $\tau < \tau_s$, a solid film with thickness $l_x > c_s \tau$ has undergone relatively little expansion during the heating time τ. This results in the buildup of pressure in a narrow region near the surface of the target, a condition known as stress confinement. In the opposite case of $l_x < c_s \tau$, the stress confinement is only partly realized, since thermal expansion is not negligible.

The formation of the stress-confined state is simulated by a combined MD/two-temperature hydrodynamics (2T-HD) approach.[21] The 2T-HD model describes the initial heating of the ions within the time of electron-ion thermalization $t \leq \tau \approx 20$ ps, while all subsequent processes leading to ablation

and spallation are described under the framework of MD. The two simulation models are linked via the one-dimensional 2T-HD electron-ion equilibrium temperature profile $T_0(x)$ at $t=\tau$, which is imposed by Langevin thermostating of the sample during the initial stage of MD simulation, $0<t\leq 20$ ps. Additional Langevin forces $\mathbf{F}_k$

$$\mathbf{F}_k = \xi_k - \beta \mathbf{v}_k \tag{1}$$

are added to the equations of motion for each atom k, where ξ_k is a Gaussian-distributed random force, and $-\beta \mathbf{v}_k$ is a frictional damping term. Two parameters, variance $\langle \xi^2 \rangle$ and friction coefficient β, must be carefully chosen in order to accurately reproduce the temperature profile within the sample after electron-ion thermalization. This is accomplished by setting these parameters such that the conditions $\langle \xi^2 \rangle = 2\beta T_0(x)/h$ and $m/\beta = \tau_{ie}$ are satisfied, where h is the MD time step and m is atomic mass. The last condition leads to time evolution of the temperature in MD as $T(t)=T_0[1-\exp(-t/\tau_{ie})]$, which is similar to $T(t)$ obtained from 2T-HD without taking into account adiabatic expansion. However, due to the relatively long electron-ion thermalization time of gold, ~20 ps, material expansion due to Langevin heating during first stage of MD simulation cannot be entirely ignored. In order to avoid nonphysical deceleration of material expanding in the x direction, only y and z components of $\mathbf{F}_k$ are applied to each atom k. The heating of x components of atomic velocities takes place via very fast energy exchange between x and y, z translational degrees of freedom in atom-atom collisions.

The 2T-HD temperature profile at $t=20$ ps, $T_0(x)$, has two characteristic components—a sharp short-range contribution localized within the heating depth d_{T_1}, and a weak long-range shoulder distributed within a layer of thickness d_{T_2}. $T_0(x)$ is approximated by a sum of two Gaussian functions

$$T_0(x) = T_1[ae^{-x^2/d_{T_1}^2} + (1-a)e^{-x^2/d_{T_2}^2}] + 300, \tag{2}$$

where T_1 is related to the surface temperature at $t=\tau$, $T_s = T_1 + 300$ K, the secondary heating depth $d_{T_2} \simeq 460$ nm, and the fitting coefficient $a \simeq 0.58$. The significant uncertainty in the electron-ion energy exchange coefficient α and the electron thermal conductivity coefficient κ in the warm dense state of metals[21] results in some uncertainty in the main heating depth, $d_{T_1} = 120-240$ nm. Therefore, due to its weak dependence on absorbed fluence, this parameter d_{T_1} was fixed to 210 nm by matching the simulated crater depth of 106 nm to the experimental value of 110 ± 10 nm. Ultimately, the validation of the entire simulation scheme is achieved by calculating the absorbed fluence threshold required to produce this crater and then comparing it to experiment.

One of the most important requirements for realistic MD simulations of usLP interactions with matter is the availability of accurate interatomic potentials suitable for simulation of materials at extreme conditions. To this end, we employed an embedded atom method (EAM) potential for gold that has been recently developed specifically to simulate materials response to a wide range of compressive and tensile stresses.[14] The fitting database for this potential included experimental data at ambient conditions: cohesive energy, lattice constant, elastic constants and bulk modulus, and first-principles cold pressure curves for high compression and tensile states of gold obtained by density-functional theory. The independently calculated melting temperature of the new EAM potential, $T_m \sim 1330$ K, is in good agreement with the experimental value of 1337.33 K.[22] As a further check on the robustness of the new EAM potential to describe the complex void formation processes that occur during ablation and spallation, the vacancy formation E_{vf} and vacancy migration E_{vm} energies were calculated and found to be in good agreement with experiment: $E_{vf}^{\mathrm{EAM}} = 0.93$ eV as compared to $E_{vf}^{exp} = 0.97 \pm 0.01$ eV,[23] and $E_{vm}^{\mathrm{EAM}} = 0.87$ eV as compared to $E_{vm}^{exp} = 0.90 \pm 0.04$ eV.[24]

In our MD simulations, the samples were perfect *fcc* crystals of gold with linear dimensions $l_x \times l_y \times l_z$ oriented in the [110] crystallographic direction along the direction of usLP. The lateral dimensions l_y and l_z were subjected to periodic boundary conditions. Small-scale simulations with crystal dimensions $1000 \times 16 \times 10$ nm^3 and number of atoms $\approx 10 \times 10^6$ were used to search for ablation and spallation thresholds while large-scale simulations with crystal dimensions $1000 \times 120 \times 16$ nm^3 and number of atoms $\approx 110 \times 10^6$ were used for production runs. Films of varying thicknesses along the transverse dimension l_x were utilized to examine ablation-spallation coupling. Possible size effects on the ablation and spallation thresholds associated with the lateral dimensions $l_y \times l_z$ of the samples were examined and found to be minor for $l_y \times l_z \geq 8 \times 8$ nm^2.

III. RESULTS

Rapid heating of the sample by usLP results in a stress-confined state, which decomposed into two oppositely traveling compression waves at the onset of material movement. The amplitudes of these waves depend on the absorbed fluence. Although for small fluences, the processes at the rear side of a thick sample can be ignored (pure ablation regime), for large enough fluences the film will be damaged on either side. The ablation process induced by the left-moving wave took place within the frontal part of the film, see Fig. 1. The spallation at the rear of the film was induced by the right-moving wave, which consisted of a long pressure wave followed by the shock front S_1, see Fig. 2. Our simulation shows that this ultrashort high-pressure wave does not cause plastic deformation and that the crystal remains in an elastic state despite being subjected to extremely high shear stresses.

A. Ablation of thick films

In the pure ablation regime, the left-moving wave was reflected at the frontal surface shortly after its formation, and transformed into a tensile wave. This wave then traveled through a segment of molten gold, which was created by the initial intense heating of the target surface layer to temperatures well above the melting point. For absorbed fluences above the cavitation threshold F_c but below the ablation threshold F_a, voids appeared during the expansion of molten material, when the tensile stress exceeds a critical value

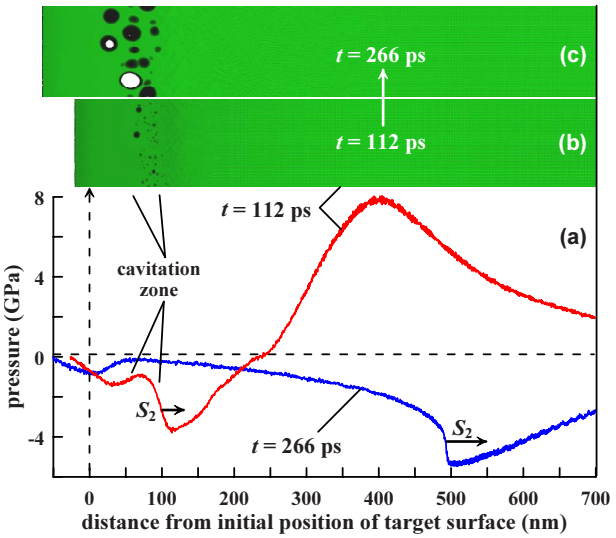

FIG. 1. (Color online) MD simulation of 1000–nm-thick gold film near the ablation threshold $F_a=137$ mJ/cm^2. Pressure profiles (a) and density maps [(b) and (c)] of the left 700 nm of the film are shown. Simultaneous nucleation of many voids in the cavitation zone produces the sharp compressive wave S_2 propagating in stretched metal and eventually transforming into a weak shock.

$\sigma_c(T)$, but collapsed shortly after nucleation, and caused no permanent damage. However, for absorbed fluences at F_a, the molten material was ruptured via simultaneous nucleation of many voids within a thin layer referred to as the cavitation zone. Some of the voids grew and coalesced forming larger bubbles while others collapsed due to the drop of surrounding tensile stress. Eventually, the largest bubble reached the lateral size of the sample, leading to detachment of a runaway ablated layer, see Ref. 25. Void nucleation caused the pressure to rise quickly to zero, resulting in the formation of a sharp compressive wave S_2, as shown in Fig. 2. As the wave propagated toward the rear surface of the sample, it steepened due to an increase in local sound speed with density within the wave front. The sharp compressive wave continued to steepen until a point at which it broke into a weak shock wave S_2. At the microscopic level, the shock wave criterion is met once the width of the wave front becomes roughly equal to several interatomic distances.[26]

In our simulations, voids appeared for the critical stress $\sigma_c \approx 2.6$ GPa, which was achieved at the cavitation threshold fluence $F_c=134$ mJ/cm^2. The cavitation zone spans a region of molten gold subjected to a high strain rate $\dot{V}/V \approx 2\times 10^8$ s^{-1}. Due to adiabatic expansion, the temperature in the molten gold, in the region where the first voids appear, rapidly dropped to 1220 K, which is 120 K below the melting temperature of gold at normal conditions. Therefore, the bubble formation takes place in supercooled liquid gold. For thick films (>0.5 μm), ablation starts to appear for an initial surface temperature $T_s=2800$ K. The calculated absorbed fluence at the ablation threshold $F_a=137$ mJ/cm^2 was found to be within the experimental range of 130–180 mJ/cm^2.[7] A source of error exists in the calculated F_a because of the finite value of the kinetic energy of the ablated layer, ≈ 3 mJ/cm^2, which results in $\sim 2\%$ uncertainty.

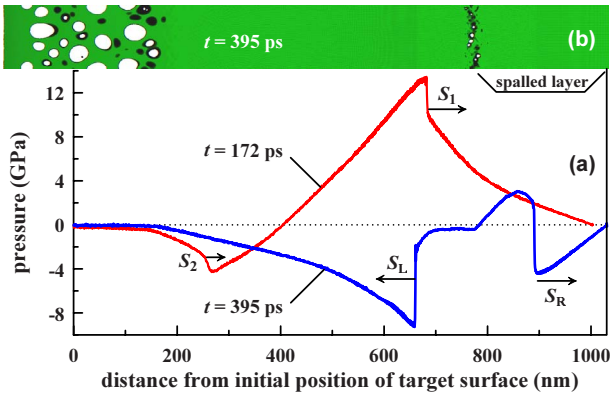

FIG. 2. (Color online) MD simulation of gold near the spallation threshold $F_s=193$ mJ/cm^2, including (a) pressure profiles and (b) density map at $t=395$ ps. The shock S_1 was formed from the initial compression wave, whereas the sharp compressive wave S_2 was produced by cavitation (see Fig. 1), and the two shocks S_L and S_R were produced by spall fracture.

B. Spallation of thick films

For usLP fluences above the ablation threshold, the right-moving compression wave formed from the initial pressurized state may cause spallation at the rear side of the film. Our simulations show that for a μ-sized sample spallation occurs for surface temperatures $T_s>3900$ K. At the spallation threshold, the absorbed fluence F_s is 193 mJ/cm^2 and the spall layer has a thickness of 250 ± 5 nm. In contrast to the ablation case, the experimental spallation threshold and spalled layer thickness for gold are unknown. Therefore, new experiments are sought to verify our predictions.

Within the spallation regime, the right-moving compression wave was transformed into the shock wave S_1 due to wave breaking, as shown in Fig. 2. The compressive wave steepens most swiftly within the portion of the wave having the largest pressure gradient and, hence, largest variation of local sound speeds. Due to the limited propagation time of the wave, controlled by the length of the film, only its top portion was able to transition to a shock, while the leading part of the wave was largely unchanged upon reflection from the rear free surface. Reflection of the S_1 from the free right surface leads to the formation of a sharp negative pressure region at the rear side of the sample. If the shear stress inside this region is large enough, the elastic-plastic transition takes place. The simulation at the spallation threshold demonstrates that this region stretches under the strain rate $\dot{V}/V \geq 6\times 10^8$ s^{-1} until the stress reaches its critical value referred to as the spall strength $\sigma^* \simeq 11.6$ GPa. At this point, the gold crystal undergoes plastic deformation and begins to fracture causing a sharp drop in stress to zero followed by the formation of the two shock waves S_L and S_R, as shown in Fig. 2. Shortly after the fracture had spread sufficiently through the sample, the part to the right of the fracture boundary detaches. Unlike ablation, where only a weak pressure wave exists within the runaway layer, the spalled layer contains a strong shock wave, which causes the velocity of the rear surface of the spalled layer to oscillate upon multiple reflections, see Fig. 3. The complete dynamics of the sample

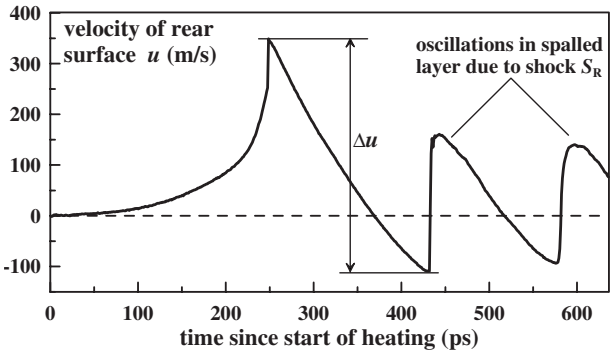

FIG. 3. Velocity of rear surface of 1-μm-thick gold film as a function of time at conditions near the spallation threshold. The velocity pullback Δu is also shown.

near the spallation threshold, including ablation in the frontal part and spallation of the rear part, are shown in Ref. 25.

In our MD simulations, the spall strength $\sigma^*=11.6$ GPa was directly obtained from the pressure profile within a simulated crystal. By analyzing the velocity of the rear surface as a function of time, we were able to compare the "true" spall strength σ^* with that calculated using the linear acoustic approximation,[10] which is routinely used for experimental estimates of σ^*. In this method

$$\sigma^* = \rho_0 c_s \Delta u/2, \tag{3}$$

where ρ_0 is the material density, c_s is the sound speed, and Δu is the velocity pullback or difference between the maximum and minimum velocities from the first peak, as shown in Fig. 3. Within the acoustic approximation, the values $\Delta u = 0.46$ km/s and $c_s=3.24$ km/s, yield $\sigma^*=14.4$ GPa which is approximately 25% greater than the true spall strength. Therefore, extreme care should be exercised when applying the acoustic approximation, Eq. (3), to calculate spall strengths of materials in experiment as such an approach might overestimate the true spall strength.

C. Ablation-spallation coupling

For thin films with thicknesses less than a few heating depths $\sim 3d_T \approx 500$ nm, but greater than the distance traveled by the sound wave during the time of electron-ion thermalization, $c_s\tau=65$ nm, the initial laser-induced heating produces a wide pressurized region spread over the entire length of the film. At the onset of material movement, this pressure profile decomposed into two transient compression waves, which were then reflected from the frontal and rear free surfaces of the target almost simultaneously. The reflected rarefaction waves travel toward the center of the target resulting in a superposition of pressures. Therefore, the target is subjected to stresses greater than those obtained by either of the individual waves, which in turn led to deformation and fracture at much lower fluences than for thicker films. In fact, in thin films, ablation and spallation are no longer spatially separated processes but constitute a single fracture phenomenon. For the cases of 100-, 200-, 300-, and 500-nm-thick films, it was found that fracture occurs at fluence thresholds 45 mJ/cm^2, 66 mJ/cm^2, 82 mJ/cm^2, and 117 mJ/cm^2, respectively, see Fig. 4. Other MD simulations of thin gold films[13,20] obtained similar fracture thresholds with one exception from the work,[15] see Fig. 4. This difference is due to the use of a small electron-ion energy exchange coefficient α, which leads to a significant increase in τ_{ie}.

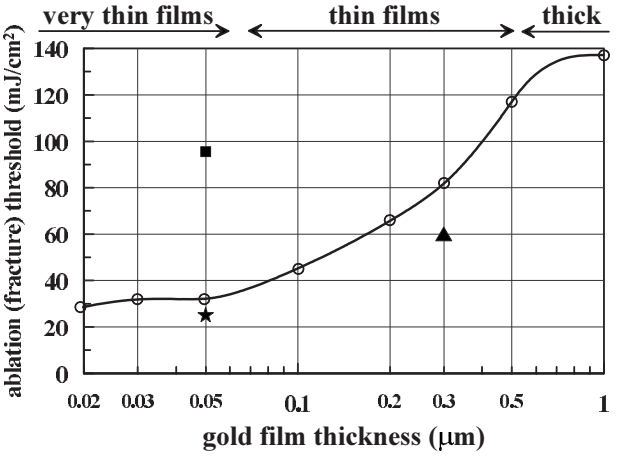

FIG. 4. Ablation/fracture threshold as a function of film thickness. Circles connected by the line are the current results, triangle from Ref. 13, square from Ref. 15, and star from Ref. 20.

In the limit of very thin films with thicknesses less than $c_s\tau=65$ nm, the thermal expansion caused by the initial heating of the crystal during electron-ion energy exchange was appreciable, thereby reducing the buildup of pressure. Thus, the stress confinement notion, which is frequently used to describe materials response to usLP, becomes less applicable in this case. As shown in Fig. 4, a very thin film required a greater absorbed energy per atom in order to reach the critical tensile stress, because absorbed fluence at the fracture threshold depends weakly on film thickness. As an example, a 20-nm-thick gold film has a fracture threshold fluence $F_a=28.5$ mJ/cm^2 that is very close to $F_a=32$ mJ/cm^2 at 50 nm but the corresponding surface temperatures are quite different: $T_s=5700$ K and $T_s=2900$ K. The temperature and pressure profiles are almost uniform in such films, and the fracture takes place at the center.

IV. CONCLUSIONS

Realistic MD simulations of μ-size samples of gold films irradiated by usLP has allowed us to obtain insights into the fundamental microscopic mechanisms of ablation and spallation, including the coupling and decoupling of spallation to and from ablation. In addition, we were able to estimate the strength of molten gold and the spall strength of solid gold at ultrahigh strain rates. Finally, good agreement between the simulated and the experimental ablation fluence

threshold provides a reliable validation of the simulated microscopic picture of materials response.

ACKNOWLEDGMENTS

This work is supported by the National Science Foundation under Grants No. DMR-0755256, No. DMR-1004873, and No. DMR-1008676. N.A.I. is supported by RFBR under Grant No. 10-08-92661-NNF_a. Simulations were performed using NSF Teragrid computers, USF Research Computing Cluster, and computational facilities of Materials Simulation Laboratory at the University of South Florida funded by ARO DURIP.

[1] *Laser Ablation and its Applications*, Springer Series in Optical Sciences Vol. 129, edited by R. Phipps (Springer, New York, 2007).
[2] S. Nolte, C. Momma, H. Jacobs, A. Tunnermann, B. N. Chichkov, B. Wellegehausen, and H. Welling, J. Opt. Soc. Am. B **14**, 2716 (1997).
[3] K. Sokolowski-Tinten, J. Bialkowski, A. Cavalleri, D. von der Linde, A. Oparin, J. Meyer-ter-Vehn, and S. I. Anisimov, Phys. Rev. Lett. **81**, 224 (1998).
[4] A. Vorobyev and C. Guo, Appl. Phys. Lett. **92**, 041914 (2008).
[5] K. Oguri, Y. Okano, T. Nishikawa, and H. Nakano, Phys. Rev. B **79**, 144106 (2009).
[6] V. V. Temnov, Ph.D. thesis, University of Duisburg-Essen, 2004.
[7] N. A. Inogamov, V. V. Zhakhovskii, S. I. Ashitkov, Yu. V. Petrov, M. B. Agranat, S. I. Anisimov, K. Nishihara, and V. E. Fortov, JETP **107**, 1 (2008).
[8] S. I. Anisimov and B. S. Luk'yanchuk, Phys. Usp. **45**, 293 (2002).
[9] S. Eliezer, E. Moshe, and D. Elieser, Laser Part. Beams **20**, 87 (2002).
[10] G. I. Kanel, S. Razorenov, and V. E. Fortov, *Shock-Wave Phenomena and the Properties of Condensed Matter* (Springer, New York, 2004).
[11] *High-Pressure Shock Compression of Solids II: Dynamic Fracture and Fragmentation*, edited by L. Davison, D. E. Grady, and M. Shahinpoor (Springer, New York, 1996).
[12] S. Amoruso, R. Bruzzese, X. Wang, N. N. Nedialkov, and P. A. Atanasov, J. Phys. D **40**, 331 (2007).
[13] Y. Gan and J. Chen, Appl. Phys. Lett. **94**, 201116 (2009).
[14] V. Zhakhovskii, N. A. Inogamov, Yu. V. Petrov, S. I. Ashitkov, and K. Nishihara, Appl. Surf. Sci. **255**, 9592 (2009).
[15] D. S. Ivanov and L. V. Zhigilei, Phys. Rev. B **68**, 064114 (2003).
[16] E. Leveugle, D. S. Ivanov, and L. V. Zhigilei, Appl. Phys. A: Mater. Sci. Process. **79**, 1643 (2004).
[17] L. V. Zhigilei, Z. B. Lin, and D. S. Ivanov, J. Phys. Chem. C **113**, 11892 (2009).
[18] L. J. Lewis and D. Perez, Appl. Surf. Sci. **255**, 5101 (2009).
[19] D. Bouilly, D. Perez, and L. J. Lewis, Phys. Rev. B **76**, 184119 (2007).
[20] Z. Lin, E. Leveugle, E. M. Bringa, and L. V. Zhigilei, J. Phys. Chem. C **114**, 5686 (2010).
[21] N. A. Inogamov, V. V. Zhakhovskii, S. I. Ashitkov, V. A. Khokhlov, Yu. V. Petrov, P. S. Komarov, M. B. Agranat, S. I. Anisimov, and K. Nishihara, Appl. Surf. Sci. **255**, 9712 (2009).
[22] D. R. Lide, *CRC Handbook of Chemistry and Physics*, 88th ed. (CRC, Boca Raton, 2007).
[23] W. Triftshäuser and J. D. McGervey, Appl. Phys. A **6**, 177 (1975).
[24] T. Kino and J. S. Koehler, Phys. Rev. **162**, 632 (1967).
[25] See supplementary material at http://link.aps.org/supplemental/10.1103/PhysRevB.82.064113 for movie: the frontal part of sample near ablation threshold, the frontal part of sample above spallation threshold, and the rear part of sample above spallation threshold.
[26] Ya. B. Zel'dovich and Yu. P. Raizer, *Physics of Shock Waves and High-Temperature Hydrodynamic Phenomena* (Dover, New York, 2002).